

Analysis of x-ray magnetic circular dichroism in the half-metallic ferromagnet CrO₂

Toshiaki Ae and Takuji Nomura*

*Department of Material Science, Graduate School of Science, University of Hyogo,
3-2-1 Kouto, Kamigori, Ako, Hyogo 678-1297, Japan*

*and Synchrotron Radiation Research Center, National Institutes for Quantum Science and Technology,
SPring-8, 1-1-1 Kouto, Sayo, Hyogo 679-5148, Japan*



(Received 30 September 2023; revised 5 January 2024; accepted 15 March 2024; published 8 May 2024)

We report a theoretical analysis of x-ray magnetic circular dichroism (XMCD) at the Cr-*L* edge in half-metallic ferromagnetic CrO₂. First, since the XMCD spectrum is the difference between the x-ray absorption spectra (XAS) for right- and left-handed circularly polarized x rays, a general perturbative method of calculating XAS spectra is developed by means of the Keldysh Green's function technique for nonequilibrium states. Subsequently, it is applied to the analysis of XMCD of half-metallic ferromagnetic CrO₂. Calculated XAS and XMCD spectra are compared with several previous experimental data. It is clearly shown that effects of the atomlike Coulomb interaction between the *2p* and *3d* states are indispensable ingredients to yield good agreement with the experiments. Such strong *2p-3d* correlation may originate from a peculiarity of the half-metallic ferromagnetic state. Evaluation of the validity of sum rules is made within our framework.

DOI: [10.1103/PhysRevB.109.184414](https://doi.org/10.1103/PhysRevB.109.184414)

I. INTRODUCTION

Half-metallic ferromagnets (HMF), where one of two spin states takes no density of states at the Fermi level, have attracted considerable attention because of basic interests in their unusual magnetic properties as well as their possible applications to spintronic devices [1–4]. CrO₂ has been a leading candidate of HMF since the first theoretical prediction by an electronic structure calculation within local density approximation (LDA) [5]. Many subsequent calculations (LDA or LDA+*U*) have supported basically this initial prediction of half-metallic ferromagnetism in CrO₂ [6–13]. Although more advanced calculations implemented with dynamical mean-field theory (DMFT) suggest emergence of the so-called nonquasiparticle states near the Fermi energy [14,15], they have not been observed experimentally in CrO₂. To confirm the realization of the half-metallic ferromagnetic state, a number of experiments have been conducted. Specifically, this includes point-contact Andreev reflection ($P = 96\%$) [16], CrO₂/I/Al junction ($P = 92\%$) [17], and a recent spin-resolved photoemission spectroscopy ($P = 100\%$ at 40 K) [18], where P is the spin-polarization ratio at the Fermi level. Assuming that experimental values of P can be reduced by imperfect sample quality, surface, or boundary conditions, we may consider these measured values of P will be sufficiently high to convince ones that complete half-metallic $P = 100\%$ should be indeed realized under ideal conditions.

X-ray magnetic circular dichroism (XMCD) has been one of the powerful tools to study magnetic properties of ferromagnets [19–22]. Particularly, for XMCD at the transition-metal *L* edge the so-called sum rules often enable one to extract selectively the transition-metal *d*-electron spin

and orbital moments, taking full advantage of element and orbital specificity in x-ray absorption spectroscopy (XAS) [23,24]. Several XMCD measurements at the Cr-*L* edge have been performed for CrO₂ in these two or three decades, and reproduced consistent spectral line shapes among them [25–30]. To explain the experimental spectral lines theoretically, several calculations of XMCD spectra have been reported. The earliest calculation is based on a ligand field multiplet (LFM) model [25], which appears to well describe the observed spectrum by assuming the atomic Cr3*d*² state. Another result of crystal-field multiplet (CFM) calculation agreeing with experimental XMCD spectral lines is found in Ref. [31]. However, the reliability of this agreement seems to be limited because of qualitative discrepancy in the underlying XAS spectrum, as seen in Sec. III A. This is not so surprising, if it is noted that CrO₂ is a metal with itinerant electrons. Thus, one will naturally expect that more accurate description should be based on an electron band picture. In fact, theoretical calculations based on first-principles electronic structures have been presented [32,33]. However, it is found that an early calculation based on the full-potential linear muffin-tin orbital (FPLMTO) method [32] shows significant deviation from experiments: first, the so-called branching ratio (BR) (L_3/L_2) in XAS is significantly larger than experimental observations. Second, the calculated XMCD spectral line as a function of absorbed photon energy appears to deviate significantly from the experimental lines. Another calculated XMCD spectral line by WIEN2K [34] appears to deviate from the experimental lines as much as the previous calculation. To resolve this difficulty in spectral line shape, Baadji and collaborators presented an explanation based on nonmagnetic natural birefringence dichroism [33].

In this study, we analyze theoretically the XMCD at the Cr-*L* edge in half-metallic ferromagnetic CrO₂. Particularly, we make an attempt to explain the XMCD spectral line shapes as well as the small BR in XAS, using accurate itinerant

*nomura.takuji@qst.go.jp

electron bands obtained by means of first-principles calculations. While we do not assume natural and birefringence dichroism, we try to take enough account of the effects of Coulomb interaction between the $2p$ core hole and excited $3d$ electrons. For our methodology, we develop a general theoretical framework based on Keldysh many-body perturbation theory for nonequilibrium states in Sec. II. Numerical calculations and comparison with previous experimental data are made for CrO_2 in Sec. III. Also, a critical evaluation of the validity of the sum rules is made from our theoretical point of view. Finally, concluding remarks are given in Sec. IV.

As a result of our study, it is shown that the $2p$ - $3d$ Coulomb interaction plays an essential role in explaining experimental spectra, and it is suggested that the previous calculations may have overlooked or underestimated the strong effects of the $2p$ - $3d$ interaction. It has been known over many years that formation of bound states (or multiple scattering) between $2p$ core hole and excited $3d$ electrons reduces the BR in XAS significantly [35–38]. Also in Ref. [32], it is mentioned that the calculation of BR in CrO_2 may be improved by including the $2p$ - $3d$ interaction. In this sense, our explanation given in this work is more conventional than the previous one based on natural birefringence dichroism. However, it is more remarkable that, to explain the experimental XMCD line shape, we need to use atomlike large values of $2p$ - $3d$ Coulomb interaction without reduction. This may be attributed to a peculiarity of the half-metallic ferromagnetic state in CrO_2 .

II. THEORY

A. Half-metallic ferromagnetic state in CrO_2

To describe the ferromagnetic ground state of CrO_2 , we carry out band structure calculations and construct tight-binding models using the maximally localized Wannier functions for Cr- d and O- p states [39–41]. CrO_2 has the tetragonal $P4_2/mnm$ structure with lattice constants $a = 4.412 \text{ \AA}$, $c = 2.916 \text{ \AA}$, and the oxygen position parameter $u = 0.303$ [42–44]. For the relevant setting to the WIEN2K band calculations, $20 \times 20 \times 20$ \mathbf{k} points, Perdew-Burke-Ernzerhof (PBE) exchange-correlation functional [45], and $R_{\text{MT}}K_{\text{max}} = 7.0$ are used, where R_{MT} and K_{max} are the smallest atomic sphere radius and the largest wave number of the plane-wave expansion of the wave function, respectively. Since the unit cell contains two Cr and four O atoms, we include 22 Wannier orbitals in total. To define the local Cr- d orbitals, we take the local Cartesian coordinate frame shown in Fig. 1. We consider two ways of describing the ferromagnetic state: (i) After performing Wannier fitting for the nonmagnetic band structure, we introduce the Hubbard-type onsite interaction at Cr site:

$$H'_{3d} = \frac{u}{2} \sum_i \sum_l \sum_{\sigma \neq \sigma'} d_{il\sigma}^\dagger d_{il\sigma'}^\dagger d_{il\sigma'} d_{il\sigma} + \frac{u'}{2} \sum_i \sum_{l \neq l'} \sum_{\sigma \sigma'} d_{il\sigma}^\dagger d_{il'\sigma'}^\dagger d_{il'\sigma'} d_{il\sigma}$$

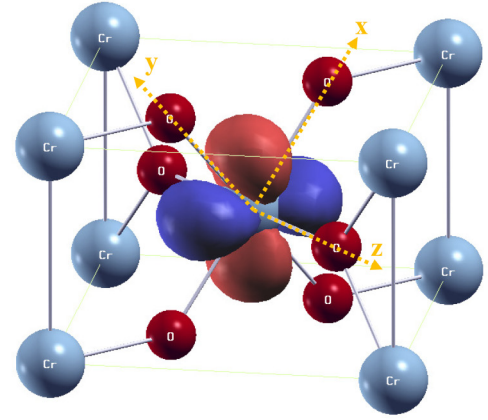


FIG. 1. Upper: Local coordinate frame and xy Wannier orbital in a unit cell of CrO_2 . Lower: Total DOS and partial DOS of Cr- d orbitals in the ferromagnetic state.

$$+ \frac{j}{2} \sum_i \sum_{l \neq l'} \sum_{\sigma \sigma'} d_{il\sigma}^\dagger d_{il'\sigma'}^\dagger d_{il\sigma} d_{il'\sigma'} + \frac{j'}{2} \sum_i \sum_{l \neq l'} \sum_{\sigma \neq \sigma'} d_{il\sigma}^\dagger d_{il'\sigma'}^\dagger d_{il'\sigma'} d_{il\sigma}, \quad (1)$$

where $d_{il\sigma}$ ($d_{il\sigma}^\dagger$) is the annihilation (creation) operator of d electron with spin σ in orbital state l (xy , xz , yz , $x^2 - y^2$, and $3z^2 - r^2$) at Cr site i . By applying mean-field approximation (MFA) to H'_{3d} with $u = 2.2 \text{ eV}$, $u' = 0.6u$, $j = j' = 0.2u$, we obtain the half-metallic ferromagnetic ground state. The one-electron energies determined by the Wannier fitting are -0.55 , -0.45 , 0.88 , and 1.02 eV for the xy , xz/yz , $x^2 - y^2$, and $3z^2 - r^2$ states, respectively, with respect to the Fermi energy. (ii) After performing GGA or GGA+ U ($U = 1, 2, 3 \text{ eV}$, $J = 0.87 \text{ eV}$) calculation with spin polarization, we obtain the half-metallic ferromagnetic state. Subsequently, we apply Wannier fitting to the spin-up and -down bands individually. In the both approaches, we include the Cr- $3d$ spin-orbit coupling by adding the term

$$H_{3d} \text{ SOC} = \xi_{3d} \sum_i \sum_{l'l''} \sum_{\sigma \sigma'} \mathbf{l}_{l'l''} \cdot \mathbf{s}_{\sigma \sigma'} d_{il\sigma}^\dagger d_{il'\sigma'} \quad (2)$$

with $\xi_{3d} = 0.047$ eV determined by an atomic calculation for Cr. Diagonalizing the 22-orbital tight-binding Hamiltonian, we have the band energies $E_a(\mathbf{k})$ and the diagonalization matrix $u_{l\sigma,a}(\mathbf{k})$, where a is band index. All of the above approaches lead to half-metallic ferromagnetic states with similar values of magnetic moment at Cr site ($2.0 \mu_B/\text{Cr}$). Previous x-ray photoemission spectroscopies suggested the presence of a peak around 1 eV, which agree with LDA+ U (3 eV) rather than plain LDA calculations [18,46–48]. However, a close comparison of band dispersion with a recent ARPES experiment [49] suggests that the MFA or GGA+ U with $U = 1$ eV is better than GGA+ U with $U \geq 2$ eV (see Supplemental Material [50]). Several previous studies suggest weak electron correlations in CrO₂ [9,13,49], while arguments on the strength of electron correlations in CrO₂ do not seem to converge yet. In addition, as we shall explain below, XMCD spectral line shapes obtained by the MFA, GGA, or GGA+ U with $U = 1$ eV are more consistent with experiments. To make the following discussions specific, we use the results based on the electron bands by MFA. Calculated density of states (DOS) within MFA is displayed in Fig. 1, and all the band structures by the above approaches are shown in the Supplemental Material [50].

B. 2p core levels

Before presenting a formula for XMCD intensity, we determine 2p core level eigenstates. In contrast to the d states, since the 2p core states are almost localized at each of transition-metal sites, we may assume completely flat dispersion for the 2p states. In this assumption, the 2p level Hamiltonian is given by

$$H_{2p} = \varepsilon_{2p} \sum_m \sum_\tau p_{m\tau}^\dagger p_{m\tau} + \xi_{2p} \sum_{mm'} \sum_{\tau\tau'} \mathbf{l}_{mm'} \cdot \mathbf{s}_{\tau\tau'} p_{m\tau}^\dagger p_{m'\tau'}, \quad (3)$$

where $m, m' = -1, 0, 1$ and $\tau, \tau' = \uparrow, \downarrow$ denote orbital magnetic quantum number and spin states, respectively, $p_{m\tau}$ is the annihilation operator for 2p _{$m\tau$} electrons, and the second term of the right-hand side is spin-orbit coupling. In this section, site index i is not explicitly shown for simplicity. H_{2p} is diagonalized easily, and the twofold-degenerate 2p_{1/2} doublets and fourfold-degenerate 2p_{3/2} quartets are obtained with the following energy eigenvalues: $\varepsilon_{2p_{1/2}} = \varepsilon_{2p} - \xi_{2p}$ and $\varepsilon_{2p_{3/2}} = \varepsilon_{2p} + \xi_{2p}/2$. In magnetic materials, the 2p levels are subject to an effective field by magnetically polarized nd electrons through the 2p- nd Coulomb interaction. The 2p- nd Coulomb interaction is expressed as

$$H_{pd} = \sum_{mm'} \sum_{\tau\tau'} \sum_{l'l'} \sum_{\sigma\sigma'} V_{pd}(m\tau, l\sigma; l'\sigma', m'\tau') p_{m\tau}^\dagger d_{l\sigma}^\dagger d_{l'\sigma'} p_{m'\tau'}, \quad (4)$$

where $V_{pd}(m\tau, l\sigma; l'\sigma', m'\tau')$ is the onsite 2p- nd Coulomb integrals. Within the mean-field level, we can consider the effective field on the 2p states by adding the following effective potential term:

$$V_{2p} = \sum_{mm'} \sum_{\tau\tau'} \sum_{l'l'} \sum_{\sigma\sigma'} V_{pd}(m\tau, l\sigma; l'\sigma', m'\tau') \times \langle d_{l\sigma}^\dagger d_{l'\sigma'} \rangle p_{m\tau}^\dagger p_{m'\tau'}, \quad (5)$$

where $\langle d_{l\sigma}^\dagger d_{l'\sigma'} \rangle$ is determined for the magnetic ground state. The actual 2p levels are determined by diagonalizing the effective Hamiltonian

$$\bar{H}_{2p} \equiv H_{2p} + V_{2p}. \quad (6)$$

Hereafter we refer to the eigenstates of \bar{H}_{2p} as 2p _{α} . The new six eigenstates are expressed by superpositions of the original 2p _{$m\tau$} states:

$$|2p_\alpha\rangle = \sum_{m=+1,0,-1} \sum_{\tau=\uparrow,\downarrow} |2p_{m\tau}\rangle u_{m\tau,\alpha}. \quad (7)$$

Thus, the degenerate 2p_{1/2} doublets and 2p_{3/2} quartets are recombined to form the six nondegenerate levels 2p _{α} in ferromagnetic states. Throughout this paper, we refer to this effect as core-level splitting (CLS).

In the calculations for CrO₂ below, we use the following parameter values: $\xi_{2p} = 5.60$ eV, $\varepsilon_{2p} = -575.9$ eV in setting the Fermi energy to zero. V_{pd} is determined using the Slater-Condon parameters, $F_{pd}^0 = 1.60$, $F_{pd}^2 = 6.52$, $G_{pd}^1 = 4.79$, $G_{pd}^3 = 2.72$ in units of eV. The values of F_{pd}^2 , G_{pd}^1 , and G_{pd}^3 are determined by the Cowan's atomic code for the configuration 2p⁵3d⁴ at Cr [60,61], since the 3d electron occupation is $N_d = 3.73$ (3.80) in the ferromagnetic (non-magnetic) state determined in Sec. II A. Here note that the d electron occupation is between Cr3d⁴ and Cr3d³ (Cr²⁺ and Cr³⁺) rather than near Cr3d² (Cr⁴⁺). Using these parameters, we obtain $\varepsilon_{2p_\alpha} = -577.51, -577.02, -569.64, -569.00, -568.23, -567.93$ in units of eV for the ferromagnetic state determined in Sec. II A.

C. Perturbative formulation of XAS

Concerning the electron-photon interaction, the relevant Hamiltonian to 2p → nd absorption is expressed as

$$H_A = \sum_{\mathbf{q}\mathbf{e}} \sum_{lm} w_{d_l, 2p_m}(\mathbf{q}\omega, \mathbf{e}) \sum_{\mathbf{k}\sigma} \gamma_{\mathbf{q}\mathbf{e}} d_{\mathbf{k}+\mathbf{q}l\sigma}^\dagger p_{\mathbf{k}m\sigma}, \quad (8)$$

where $\gamma_{\mathbf{q}\mathbf{e}}$ is the annihilation operator of absorbed photon with wave number \mathbf{q} , frequency ω , and polarization vector \mathbf{e} . $w_{d_l, 2p_m}(\mathbf{q}\omega, \mathbf{e})$ is given within the electric dipole approximation by

$$w_{d_l, 2p_m}(\mathbf{q}\omega, \mathbf{e}) = -ie\omega^{\frac{1}{2}} \langle nd_l | \mathbf{e} \cdot \mathbf{r} | 2p_m \rangle, \quad (9)$$

where e is the elementary charge, and we have used natural units, i.e., $c = \hbar = 1$ [62]. The relation $\hbar\omega = c|\mathbf{q}|$ in ordinary units is simply expressed as $\omega = |\mathbf{q}|$ in natural units. For photons with right- and left-circular polarization (RCP/LCP),

$$\mathbf{e} = \mathbf{e}_{R/L} = \frac{1}{\sqrt{2}} (\mathbf{e}_\pi \pm i\mathbf{e}_\sigma), \quad (10)$$

where \mathbf{e}_π and \mathbf{e}_σ point along the parallel and perpendicular directions to the plane of incidence, respectively.

Now we consider a process that a photon ($\mathbf{q}\omega, \mathbf{e}$) is introduced at infinite past ($t = -\infty$), and subsequently the photon is absorbed by the electron system. Within the first order in H_A , the probability amplitude of photon absorption before $t = t_0$ is given by

$$|\psi_{\mathbf{q}\mathbf{e}}(t_0)\rangle = -i \int_{-\infty}^{t_0} dt U(t_0, t) H_A U(t, -\infty) \gamma_{\mathbf{q}\mathbf{e}}^\dagger |0\rangle, \quad (11)$$

where $|0\rangle$ is the initial ground state with no photons, and $U(t, u)$ is the bare time-evolution operator unperturbed with respect to H_A . $U(t, u)$ can be decoupled in the form of a product of the time-evolution operators for the electron and photon systems:

$$U(t, u) = e^{-iH_{\text{ph}}(t-u)} e^{-iH_{\text{el}}(t-u)}, \quad (12)$$

where H_{el} is the Hamiltonian only for electrons (strongly correlated in general), and H_{ph} is the Hamiltonian only for free photons:

$$H_{\text{ph}} = \sum_{\mathbf{q}\mathbf{e}} \omega \gamma_{\mathbf{q}\mathbf{e}}^\dagger \gamma_{\mathbf{q}\mathbf{e}} \quad (13)$$

with $\omega = |\mathbf{q}|$. The probability of photon absorption is given by the square of norm of the amplitude:

$$\begin{aligned} P_{\mathbf{q}\mathbf{e}}(t_0) &= \langle \psi_{\mathbf{q}\mathbf{e}}(t_0) | \psi_{\mathbf{q}\mathbf{e}}(t_0) \rangle \\ &= \int_{-\infty}^{t_0} dt \int_{-\infty}^{t_0} dt' \langle 0 | \gamma_{\mathbf{q}\mathbf{e}} U(-\infty, t') H_A^\dagger U(t', t_0) U(t_0, t) \\ &\quad \times H_A U(t, -\infty) \gamma_{\mathbf{q}\mathbf{e}}^\dagger | 0 \rangle. \end{aligned} \quad (14)$$

XAS intensity is defined by the number of annihilated photons per unit time, and therefore obtained by differentiating $P_{\mathbf{q}\mathbf{e}}(t_0)$ in t_0 :

$$I(\mathbf{q}\omega, \mathbf{e}) = \frac{dP_{\mathbf{q}\mathbf{e}}(t_0)}{dt_0}. \quad (15)$$

By substituting Eq. (14) into (15), contracting the photon creation and annihilation operators, and then taking the limit $t_0 \rightarrow \infty$, we have the following expression of XAS intensity:

$$I(\mathbf{q}\omega, \mathbf{e}) = \int_{-\infty}^{\infty} ds A_{\mathbf{q}\mathbf{e}}(s) e^{i\omega s}, \quad (16)$$

where $A_{\mathbf{q}\mathbf{e}}(s)$ is given by

$$A_{\mathbf{q}\mathbf{e}}(t' - t) = \langle 0 | T_K [\tilde{H}_{\mathbf{q}\mathbf{e}}^\dagger(t') \tilde{H}_{\mathbf{q}\mathbf{e}}(t)] | 0 \rangle. \quad (17)$$

Here $T_K[\dots]$ means a time-ordered product along the so-called Keldysh contour [63]. $\tilde{H}_{\mathbf{q}\mathbf{e}}(t)$ is given by

$$\tilde{H}_{\mathbf{q}\mathbf{e}}(t) = e^{iH_{\text{el}}t} \tilde{H}_{\mathbf{q}\mathbf{e}} e^{-iH_{\text{el}}t}, \quad (18)$$

with

$$\tilde{H}_{\mathbf{q}\mathbf{e}} = \sum_{lm} \sum_{\mathbf{k}\sigma} w_{d_l, 2p_m}(\mathbf{q}\omega, \mathbf{e}) a_{\mathbf{k}+\mathbf{q}l\sigma}^\dagger p_{\mathbf{k}m\sigma}. \quad (19)$$

$A_{\mathbf{q}\mathbf{e}}(t' - t)$ can be calculated perturbatively by using the Keldysh diagrammatic technique for nonequilibrium many-electron systems. We may safely assume that only a single pair of $2p$ hole and nd electron remains in the final state since such processes dominantly contribute to the XAS intensity. Under this assumption, the XAS diagram becomes Fig. 2(a), where the shaded triangle represents the electron-photon interaction vertex which is generally renormalized by electron correlations. Hereafter, we use shorthand notation like $l\sigma \equiv \zeta$, $l'\sigma' \equiv \zeta'$ for d electron states. The XAS intensity is given

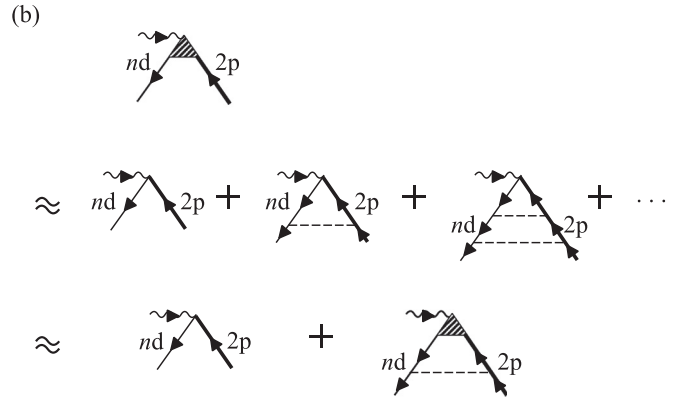
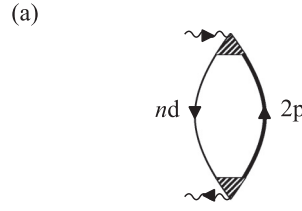


FIG. 2. (a) Diagrammatic representation of the $2p \rightarrow nd$ XAS intensity. Wavy, thick, and thin lines represent the propagators (Green's functions) of photon, core $2p$, and conduction nd electrons, respectively. Shaded triangular vertex represents a renormalized electron-photon interaction. (b) Ladder vertex correction for the electron-photon interaction vertex. Dashed lines represent the $2p$ - nd Coulomb interaction.

by

$$\begin{aligned} I(\mathbf{q}\omega, \mathbf{e}) &= \sum_{\alpha\zeta\zeta'} W_{d_{\zeta'}, 2p_\alpha}^*(\mathbf{q}\omega, \mathbf{e}) W_{d_\zeta, 2p_\alpha}(\mathbf{q}\omega, \mathbf{e}) \\ &\quad \times \frac{1}{N} \sum_{\mathbf{k}} \int_{-\infty}^{\infty} \frac{d\varepsilon}{2\pi} G_{2p_\alpha}^+(\varepsilon) G_{\zeta'\zeta}^-(\mathbf{k}, \varepsilon + \omega), \end{aligned} \quad (20)$$

where $G_{2p_\alpha}^+(\varepsilon)$ and $G_{\zeta'\zeta}^-(\mathbf{k}, \varepsilon)$ are the Keldysh Green's functions for the $2p$ and nd electrons, respectively. $W_{d_\zeta, 2p_\alpha}(\mathbf{q}\omega, \mathbf{e})$ is a renormalized vertex, which is different from the bare $w_{d_l, 2p_m}(\mathbf{q}\omega, \mathbf{e})$. For $G_{2p_\alpha}^+(\varepsilon)$ and $G_{\zeta'\zeta}^-(\mathbf{k}, \varepsilon)$, we use the explicit form

$$G_{2p_\alpha}^+(\varepsilon) = 2\pi i \delta(\varepsilon - \varepsilon_{2p_\alpha}), \quad (21)$$

$$G_{\zeta'\zeta}^-(\mathbf{k}, \varepsilon) = -2\pi i \sum_a u_{\zeta', a}(\mathbf{k}) u_{\zeta, a}^*(\mathbf{k}) [1 - n_{a\mathbf{k}}] \delta[\varepsilon - E_a(\mathbf{k})], \quad (22)$$

where $n_{a\mathbf{k}}$ is the electron occupancy of the a th band at \mathbf{k} and $u_{\zeta, a}(\mathbf{k})$ is the d_ζ -electron element of diagonalization matrix. Substituting Eqs. (21) and (22) into (20), we have

$$\begin{aligned} I(\mathbf{q}\omega, \mathbf{e}) &= 2\pi \sum_{\alpha\zeta\zeta'} W_{d_{\zeta'}, 2p_\alpha}^*(\mathbf{q}\omega, \mathbf{e}) W_{d_\zeta, 2p_\alpha}(\mathbf{q}\omega, \mathbf{e}) \\ &\quad \times \sum_{a\mathbf{k}} u_{\zeta', a}(\mathbf{k}) u_{\zeta, a}^*(\mathbf{k}) [1 - n_{a\mathbf{k}}] \\ &\quad \times \delta[\varepsilon_{2p_\alpha} + \omega - E_a(\mathbf{k})]. \end{aligned} \quad (23)$$

The XAS and XMCD intensities are calculated by

$$I(\mathbf{q}\omega) = I(\mathbf{q}\omega, \mathbf{e}_R) + I(\mathbf{q}\omega, \mathbf{e}_L), \quad (24)$$

$$\Delta I(\mathbf{q}\omega) = I(\mathbf{q}\omega, \mathbf{e}_R) - I(\mathbf{q}\omega, \mathbf{e}_L). \quad (25)$$

For the purpose of discussions on sum rules, we define the integrated XAS and XMCD intensities:

$$S[\omega_1, \omega_2] \equiv \int_{\omega_1}^{\omega_2} d\omega I(\mathbf{q}\omega), \quad (26)$$

$$\Delta S[\omega_1, \omega_2] \equiv \int_{\omega_1}^{\omega_2} d\omega \Delta I(\mathbf{q}\omega). \quad (27)$$

By setting ω_1 and ω_2 to the lowest- and highest-energy cutoffs, respectively, to cover both the L_3 and L_2 weights, we have the total integrated XAS intensity $S_L \equiv S[\omega_1, \omega_2]$ and the integrated XMCD intensity from the lowest energy $\Delta S(\omega) \equiv \Delta S[\omega_1, \omega]$. By restricting the integration range $[\omega_1, \omega_2]$ to just cover the L_3 or L_2 excitation energy, we have the partial integrated XAS and XMCD intensities for the L_3/L_2 excitations:

$$S_{L_3/L_2} \equiv S[\omega_1, \omega_2], \quad (28)$$

$$\Delta S_{L_3/L_2} \equiv \Delta S[\omega_1, \omega_2]. \quad (29)$$

In terms of the sum rules [23,24], these integrated intensities are related to various moments of d electrons:

$$\frac{\Delta S_{L_3} + \Delta S_{L_2}}{S_L} = -\frac{3L_Z}{4H_d}, \quad (30)$$

$$\frac{-\Delta S_{L_3} + 2\Delta S_{L_2}}{S_L} = \frac{2S_Z + 7T_Z}{2H_d}, \quad (31)$$

where H_d is the total hole number of d states, L_Z , S_Z , and T_Z are the [001] components of orbital, spin, and magnetic dipole moments of the d electrons, respectively. In this paper, the components along the crystallographic [100], [010], and [001] directions are denoted by X , Y , and Z , respectively. The propagation vector \mathbf{q} of incident photons is always set to be parallel to the magnetization \mathbf{M} .

$$W_{d_\zeta, 2p_\alpha}(\mathbf{q}\omega, \mathbf{e}) = w_{d_\zeta, 2p_\alpha}(\mathbf{q}\omega, \mathbf{e}) - \sum_{\alpha'\zeta_1\zeta_2} W_{d_{\zeta_2}, 2p_{\alpha'}}(\mathbf{q}\omega, \mathbf{e}) \frac{1}{N} \sum_{\mathbf{a}\mathbf{k}} \frac{u_{\zeta_1, a}(\mathbf{k})u_{\zeta_2, a}^*(\mathbf{k})[1 - n_{\mathbf{a}\mathbf{k}}]}{\omega + \varepsilon_{2p_{\alpha'}} - E_a(\mathbf{k}) + i\Gamma_{2p}} V_{pd}(\alpha', \zeta; \zeta_1, \alpha). \quad (32)$$

Thus, $W_{d_\zeta, 2p_\alpha}(\mathbf{q}\omega, \mathbf{e})$ within LVC is obtained by solving

$$\sum_{\alpha'\zeta_2} \left\{ \delta_{\alpha\alpha'} \delta_{\zeta\zeta_2} + \sum_{\zeta_1} \frac{1}{N} \sum_{\mathbf{a}\mathbf{k}} \frac{u_{\zeta_1, a}(\mathbf{k})u_{\zeta_2, a}^*(\mathbf{k})[1 - n_{\mathbf{a}\mathbf{k}}]}{\omega + \varepsilon_{2p_{\alpha'}} - E_a(\mathbf{k}) + i\Gamma_{2p}} V_{pd}(\alpha', \zeta; \zeta_1, \alpha) \right\} W_{d_{\zeta_2}, 2p_{\alpha'}}(\mathbf{q}\omega, \mathbf{e}) = w_{d_\zeta, 2p_\alpha}(\mathbf{q}\omega, \mathbf{e}). \quad (33)$$

The XMCD spectral intensity with LVC is calculated using this corrected $W_{d_\zeta, 2p_\alpha}(\mathbf{q}\omega, \mathbf{e})$ in Eq. (23). If we neglect the effects of LVC, we use the bare $w_{d_\zeta, 2p_\alpha}(\mathbf{q}\omega, \mathbf{e})$ instead of $W_{d_\zeta, 2p_\alpha}(\mathbf{q}\omega, \mathbf{e})$.

III. RESULTS

A. XAS spectra

Before discussing XMCD, we make a comparison of XAS spectral line shape with experiments to check the validity of

D. Ladder vertex correction

It has been known that in transition-metal L -edge XAS, $2p$ - nd Coulomb interaction plays an essential role to yield good agreement with experiment [35–37]. Physically, this means $2p$ - nd Coulomb interaction causes a bound state between the excited $2p$ hole and nd electron. We include this effect by the ladder vertex correction (LVC). To do this, we collect the contributions from the diagrammatic series shown in Fig. 2(b), and obtain the following equation to determine the corrected $W_{d_\zeta, 2p_\alpha}(\mathbf{q}\omega, \mathbf{e})$:

$$W_{d_\zeta, 2p_\alpha}(\mathbf{q}\omega, \mathbf{e}) = w_{d_\zeta, 2p_\alpha}(\mathbf{q}\omega, \mathbf{e}) + i \sum_{\alpha'\zeta_1\zeta_2} W_{d_{\zeta_2}, 2p_{\alpha'}}(\mathbf{q}\omega, \mathbf{e}) \int_{-\infty}^{\infty} \frac{d\varepsilon}{2\pi} G_{2p_{\alpha'}}^c(\varepsilon) \times \frac{1}{N} \sum_{\mathbf{k}} G_{\zeta_1\zeta_2}^c(\mathbf{k}, \varepsilon + \omega) V_{pd}(\alpha', \zeta; \zeta_1, \alpha), \quad (34)$$

where $w_{d_\zeta, 2p_\alpha}(\mathbf{q}\omega, \mathbf{e})$ is the bare part:

$$w_{d_\zeta, 2p_\alpha}(\mathbf{q}\omega, \mathbf{e}) = \sum_{m=-1,0,1} w_{d_\zeta, 2p_m}(\mathbf{q}\omega, \mathbf{e}) u_{m\sigma, \alpha}. \quad (35)$$

$G_{2p_\alpha}^c(\mathbf{k}, \varepsilon)$ and $G_{\zeta_1\zeta_2}^c(\mathbf{k}, \varepsilon)$ are the usual causal Green's functions: for the $2p$ states,

$$G_{2p_\alpha}^c(\mathbf{k}, \varepsilon) = \frac{1}{\varepsilon - \varepsilon_{2p_\alpha} - i\Gamma_{2p}}, \quad (36)$$

and for the nd states,

$$G_{\zeta_1\zeta_2}^c(\mathbf{k}, \varepsilon) = \sum_a u_{\zeta_1, a}(\mathbf{k}) u_{\zeta_2, a}^*(\mathbf{k}) G_a^c(\mathbf{k}, \varepsilon), \quad (37)$$

$$G_a^c(\mathbf{k}, \varepsilon) = \frac{1 - n_{\mathbf{a}\mathbf{k}}}{\varepsilon - E_a(\mathbf{k}) + i\delta} + \frac{n_{\mathbf{a}\mathbf{k}}}{\varepsilon - E_a(\mathbf{k}) - i\delta}. \quad (38)$$

The $2p$ - nd interaction $V_{pd}(\alpha', \zeta; \zeta', \alpha)$ is related to $V_{pd}(m\sigma, \zeta; \zeta', m'\sigma')$ appearing in Eq. (4) by

$$V_{pd}(\alpha', \zeta; \zeta', \alpha) = \sum_{mm'} \sum_{\sigma\sigma'} V_{pd}(m\sigma, \zeta; \zeta', m'\sigma') u_{m\sigma, \alpha}^* u_{m'\sigma', \alpha}. \quad (39)$$

By substituting Eqs. (34)–(36) into (32) and carrying out the frequency integration, we have

calculations because the XMCD intensity is the difference between the XAS intensities for right and left helicities. Here it should be noted that CrO_2 is a metastable state at room temperature in the atmosphere and its surface tends to be coated with Cr_2O_3 [58]. Therefore, we need to be careful in

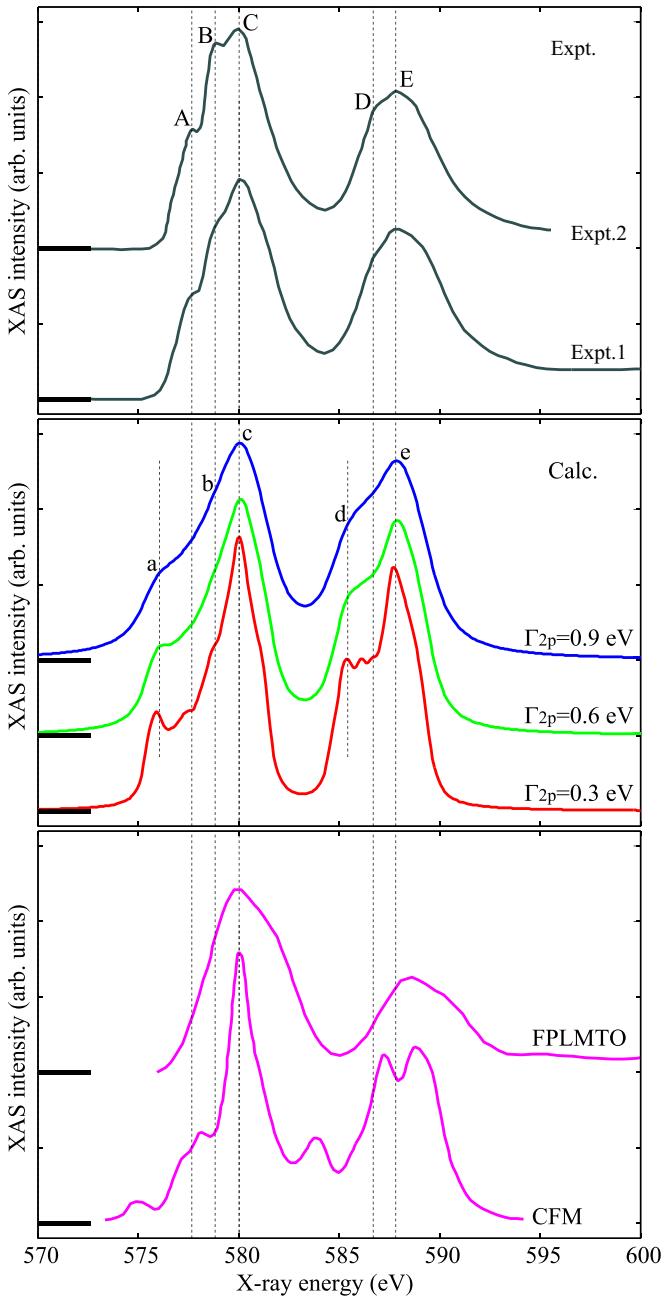


FIG. 3. Comparison of results of XAS intensity. Upper: Two experimental curves. The Expt. 1 and Expt. 2 curves are reproduced from Refs. [26] and [58], respectively. Middle: Calculated results in this work. The three curves are for different values of $\Gamma_{2p} = 0.3, 0.6, 0.9$ eV. Lower: Results of previous CFM and FPLMTO calculations, reproduced from Refs. [31] and [32], respectively. All the curves are horizontally shifted from the original energy positions to align the main L_3 peak positions exactly to that of the Expt. 1 curve. Each thick horizontal bar at the left-hand side indicates the baseline for the corresponding curve.

comparing with experimental XAS spectra. In the upper panel of Fig. 3, two experimental XAS lines are reproduced from Refs. [26,58]. The deviation of the Expt. 1 curve from the Expt. 2 curve could possibly be attributed to surface Cr_2O_3 since the Expt. 2 curve contains only a negligible (if at all)

contribution of a Cr_2O_3 signal according to Ref. [58]. However, we note that the energy positions of the five features denoted as A–E seem much consistent between the two experimental spectra. Therefore, we assume those five features are intrinsic for CrO_2 and their energy positions are quantitatively reliable. For reference, the XAS spectrum of antiferromagnetic Cr_2O_3 calculated within the present framework is given in the Supplemental Material [50], where we find five spectral features corresponding to a–e as well as in CrO_2 .

In the middle panel of Fig. 3, calculated XAS spectra $I(\mathbf{q}\omega)$ are displayed for three values of Γ_{2p} . The five features A–E are assigned well to the five features a–e in the calculated curves, although it is somewhat uncomfortable that the feature b (only visible for $\Gamma_{2p} = 0.3$ eV) is much weaker than B and the features a and d appear at lower energy than A and D by about 1 eV, respectively. The BR defined by S_{L_3}/S_{L_2} is estimated to be 1.11 in the present calculation, showing significant reduction from the statistical value 2. This value should be compared with an experimental value 1.24, which is estimated from the integrated XAS curve in Ref. [26]. As has been discussed by many authors, this reduction can be explained as an effect of $2p$ - $3d$ interaction [35–38]. As seen later in Sec. III D, the BR calculated without CLS and LVC is exactly 2.00, which clearly disagrees with experiments.

Here we insert a comment on the effects of the relaxation factor Γ_{2p} . Although we treat Γ_{2p} as constant in absorbed x-ray energy for simplicity in this study, we have to consider that Γ_{2p} acquires an energy dependence in more elaborate calculations. In a more microscopic level, since Γ_{2p} corresponds to the imaginary part of the $2p$ -state self-energy arising from relaxation processes of the $2p$ hole, such processes should be identified and included in the calculations explicitly. Previously, such relaxation processes were considered within lowest-order perturbative calculations for the $K\alpha$ emission (XES) and its circular dichroism (XMCD) in ferromagnetic transition metals, leading to asymmetric XES line shape with characteristic broad tail structures [64,65]. As well as in the XES calculations, the energy dependence of the imaginary part of the $2p$ self-energy can change each broadness, asymmetry, and intensity height of the features a–e individually, thereby possibly yielding some correction to the calculated XAS line shape.

Finally, in the bottom panel of Fig. 3, the results of the previous CFM and FPLMTO calculations [31,32] are displayed for comparison. The CFM result shows qualitative discrepancy with the experimental lines: A preedge peak around 575 eV and a peak around 584 eV between the L_3 and L_2 weights are seen, while such structures are absent in experimental spectra as well as in the band-based spectra.

B. XMCD spectra

In the upper panel of Fig. 4, calculated helicity-resolved XAS spectra $I(\mathbf{q}\omega, \mathbf{e}_{R/L})$ are compared with the experimental results of Ref. [26]. We have taken small $\Gamma_{2p} = 0.3$ eV to make inherent structures visible, although they may be actually invisible in experiments. In the lower panel of Fig. 4, calculated XMCD spectral intensity $\Delta I(\mathbf{q}\omega)$ and its integrated intensity $\Delta S(\omega)$ are compared with the experiment. Here we note that the XMCD spectra can less possibly contain a

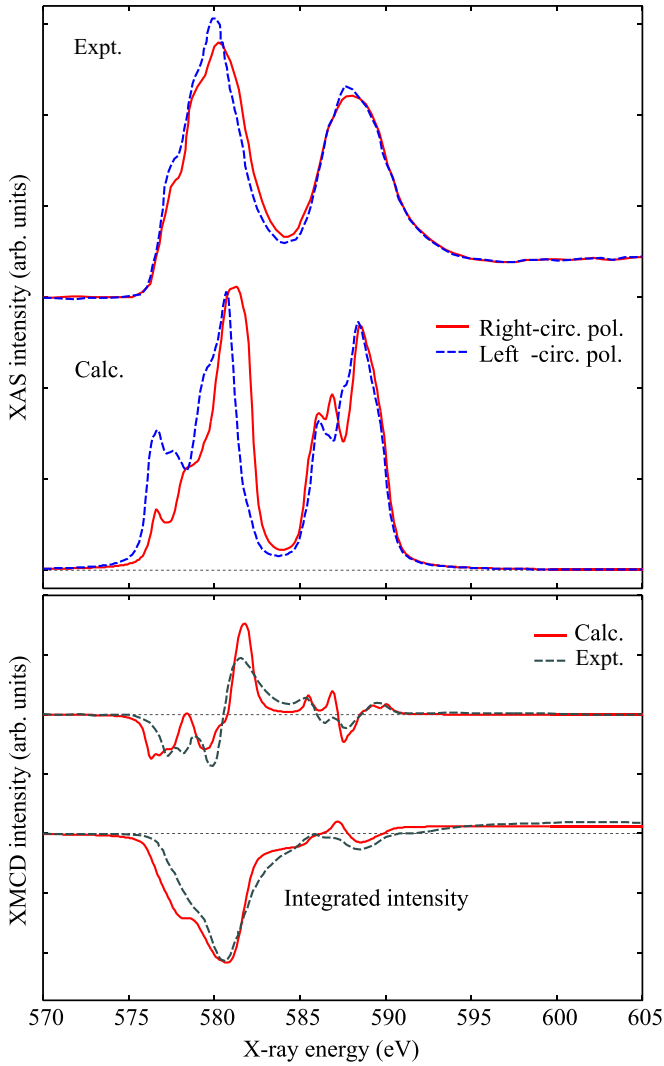


FIG. 4. Upper: Experimental and calculated XAS spectra for RCP/LCP. The L_3 and L_2 XAS peaks are located around 580- and 588-eV excitation energies, respectively. Lower: XMCD spectrum $\Delta I(\mathbf{q}\omega)$ and integrated intensity $\Delta S(\omega)$. Experimental data are read from Ref. [26].

contribution from surface Cr_2O_3 since Cr_2O_3 is an antiferromagnet and therefore its contribution will be eliminated by taking the difference between the helicity-resolved XAS spectra. The calculated curves overall agree well with the experiment. However, still some deviations are seen: (i) First, the horizontal position of the first low-energy dip around 576–577 eV is lower by 1 eV than in the experiment. (ii) Compared with the experiment, the dip around 580 eV is shallower, and the peak around 581–582 eV is higher. In other words, both the dip and peak structures in the calculation deviate upward from the experimental ones. (iii) The small peak around 586–587 eV takes a positive value at the local maximum, although it should be negative according to the experiment. These deviations seem to arise from those in positions and intensities of peaks and fine features in XAS spectra. For example, the deviation (i) originates from the deviation in energy positions between the features A and a in the underlying XAS spectra given in Sec. III A. The deviation (ii) arises from the following

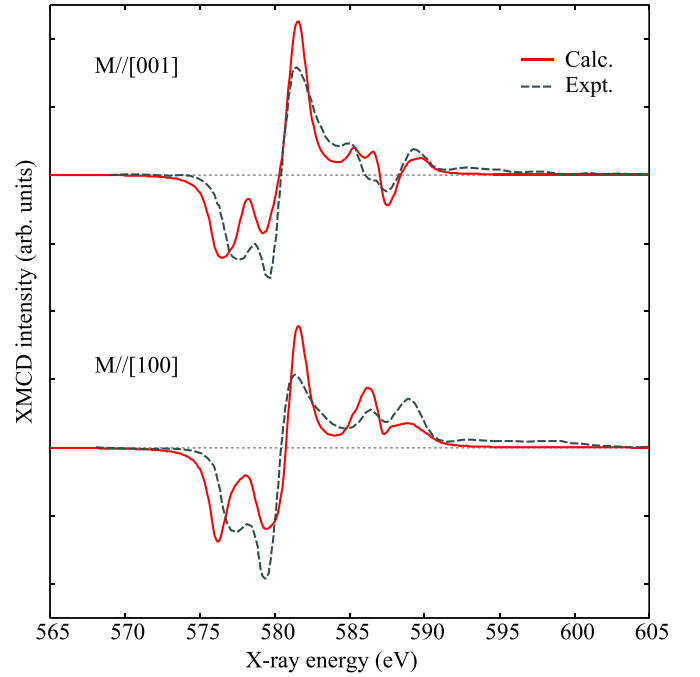


FIG. 5. XMCD spectra for different cases of magnetization direction, $\mathbf{M}/[001]$ and $\mathbf{M}/[100]$. For the calculation, we used $\Gamma_{2p} = 0.6$ eV. Experimental data are read from Ref. [27].

difference between the calculation and the experiment: the maximum intensity at the L_3 XAS peak is almost the same between RCP and LCP in the calculation, although it is clearly higher for LCP than for RCP in the experiment. Origins of these incompatibilities are not clear at present. Inaccuracy not only in the electronic structure but in the approximate treatment of XAS can be responsible for them.

XMCD spectra based on the band structures by GGA and GGA+ U are displayed in the Supplemental Material [50]. The XMCD line shapes by GGA and GGA+ U with $U \leq 1$ eV appear to be similar to those of MFA, keeping agreement with experiments. On the other hand, for larger $U \geq 2$ eV, discrepancies with experiments become noticeable: Relative depth of the first dip around 576–577 eV to the second dip at 580 eV becomes larger. In addition, the XMCD curve tends to have a negative dip around 585 eV. Thus, if GGA+ U with $U \geq 2$ eV is used, compatibility in spectral line shape with experiments becomes worse.

C. Anisotropy of XMCD spectra

The XMCD spectrum has been observed to show a characteristic dependence on the direction of magnetization [27,28]. As shown in Fig. 5, the XMCD line shows a notable change in sign from negative for $\mathbf{M}/[001]$ to positive for $\mathbf{M}/[100]$ around 588 eV. The calculation reproduces well this sign change. We investigate which electron excitations are responsible for the sign change around this energy, by allowing only one of the five Cr-3d orbitals to accept electrons and suppressing the others. This investigation shows that the negative sign for $\mathbf{M}/[001]$ originates from the excitations relevant to the Cr- $3d_{3z^2-r^2}$ orbital. In the case of $\mathbf{M}/[001]$, this negative sign is dominantly reflected in the total XMCD line. On the other

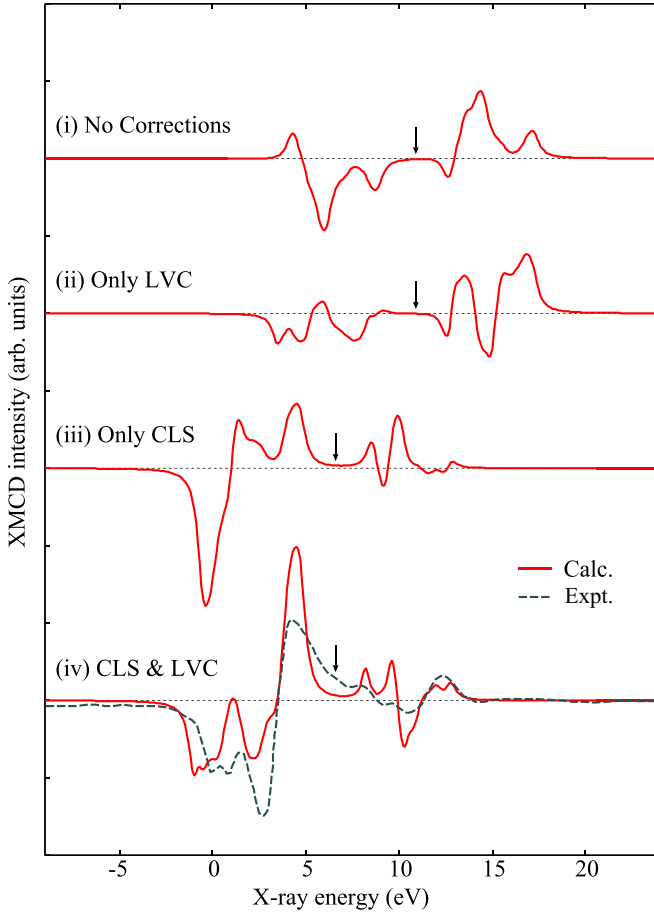


FIG. 6. From top to bottom, solid curves represent the XMCD spectra calculated with (i) no corrections, (ii) only LVC, (iii) only CLS, and (iv) full corrections (CLS and LVC). Dashed curve represents experimental data read from Ref. [25]. Downward arrows indicate the minimum position between the calculated L_3 and L_2 XAS peaks, where the L_3 and L_2 excitations are assumed to be separated.

hand, in the case of $\mathbf{M}//[100]$, the $3d_{xy}$ orbital brings about a dominant positive contribution to overcome the negative contribution from the $3d_{3z^2-r^2}$ orbital. The tendency to this sign change is reproduced also within the GGA and GGA+ U calculations [50].

Concerning the anisotropy of moments, the orbital and spin moments are very isotropic: L_Z for $\mathbf{M}//[001]$ and L_X for $\mathbf{M}//[100]$ are both -0.033 , and S_Z for $\mathbf{M}//[001]$ and S_X for $\mathbf{M}//[100]$ are both 1.032 per Cr atom. On the other hand, the magnetic dipole moment exhibits some anisotropy: T_Z for $\mathbf{M}//[001]$ and T_X for $\mathbf{M}//[100]$ are -0.077 and 0.039 , respectively. These results do not agree with the large anisotropy stressed in Ref. [27], but are consistent with LSDA(+OP) calculation [66] in the order of magnitude and sign.

D. Effects of $2p$ - $3d$ interaction on XMCD spectra

To inspect the effects of $2p$ - $3d$ interaction, we present the XMCD spectral line shapes calculated with and without CLS and LVC in Fig. 6. If we omit either of the CLS and LVC corrections, we cannot obtain agreement with

experiments. On the other hand, it should be noted that the spectral line shape without both the CLS and LVC corrections (the top curve in Fig. 6) is very similar to those obtained in Refs. [32,34]. Therefore, the previous XMCD calculations based on the first-principles calculations may have overlooked or underestimated the effects of the $2p$ - $3d$ interaction both in the description of $2p$ core-level splitting (CLS) and $2p$ - $3d$ bound-state formation (LVC). While the MFA and GGA+ U with $U \leq 1$ eV both give similar XMCD spectral line shapes as already mentioned in Sec. III B, the CLS and LVC both give a strong influence on the XMCD spectral line shape. This means clearly that the careful description of the $2p$ - $3d$ correlations is much more crucial for explaining the experimental spectra than the improvement of the $3d$ electron bands.

To see the influence of the $2p$ - $3d$ interaction on the BR and XMCD integrated intensity, the calculated values of them are listed in the lower five lines of Table I. Excitation energy separating the L_3 and L_2 spectral weights is determined by the position of the local minimum between the L_3 and L_2 peaks of XAS spectrum. According to the results, the reduction of BR arises mainly from LVC and not from CLS. On the other hand, the relative weight of dichroism to the whole XAS weight $\Delta S_{L_3/L_2}/S_L$ becomes much suppressed by either of CLS and LVC.

E. Evaluation of sum rules

The sum rules have often been utilized to extract the local orbital and spin moments at magnetic ions in solids. This unique advantage has distinguished XMCD from other experimental techniques on magnetism. Extraction of the moments by the sum rules has sometimes been successful for late $3d$ transition elements such as Fe, Ni, and Co, where the $2p$ spin-orbit coupling is sufficiently large to separate the L_3 and L_2 weights clearly [67–71]. However, for middle and early $3d$ transition elements where the L_3 - L_2 separation is not so large, the validity and accuracy of the sum rules have sometimes been questioned [20,70–72]. To examine the validity of the sum rules in the case of CrO_2 , we summarize the calculated results of the relevant moments and the right- and left-hand sides of Eqs. (30) and (31) in Table I. As seen in Table I, the orbital sum rule [Eq. (30)] holds well, even if CLS and LVC are included. On the other hand, the spin sum rule [Eq. (31)] is violated by including CLS and LVC. In general, the orbital sum rule holds robustly, compared with the spin sum rule, because of the following reason: Only what is necessary for the orbital sum rule to hold is that the space formed by the total six $2p_\alpha$ states is formed equivalently by the original $2p_{m\tau}$ states. This is clearly satisfied robustly. On the other hand, for the spin sum rule to hold, the two spaces formed by the low-energy two (L_2) and the high-energy four (L_3) of the six $2p_\alpha$ states need to be formed individually by the $2p_{1/2}$ and $2p_{3/2}$ states, respectively. Not only CLS but LVC violates this requirement, since CLS causes hybridization between the $2p_{1/2}$ and $2p_{3/2}$ states in the ground state and the LVC processes include dynamical transitions between them.

If we apply the spin sum rule to the calculated XMCD intensity, then the value of $S_Z + (7/2)T_Z$ is excessively underestimated, as explained in the following. If we use the values of H_d , $\Delta S_{L_3}/S_L$, and $\Delta S_{L_2}/S_L$ in Table I, then we expect

TABLE I. Upper two lines: calculated values of the d -electron (-hole) number N_d (H_d) and various moments of orbital L_Z , spin S_Z , and magnetic dipole T_Z , per Cr atom. For the moments, the [001] components are shown. Lower five lines: calculated branching ratio (BR) and integrated XMCD intensities normalized by the total integrated XAS intensity. In the two columns of the right-hand side, calculated values of the right- and left-hand sides of Eqs. (30) and (31) are shown in boldface.

N_d (H_d)	L_Z	S_Z	T_Z	$-\frac{3L_Z}{4H_d}$	$\frac{2S_Z+7T_Z}{2H_d}$
3.73 (6.27)	-0.033	1.032	-0.077	0.00395	0.121
	BR $\left(\frac{S_{L_3}}{S_{L_2}}\right)$	$\frac{\Delta S_{L_3}}{S_L}$	$\frac{\Delta S_{L_2}}{S_L}$	$\frac{\Delta S_{L_3} + \Delta S_{L_2}}{S_L}$	$\frac{-\Delta S_{L_3} + 2\Delta S_{L_2}}{S_L}$
(i) No corrections	2.00	-0.0355	0.0395	0.00393	0.114
(ii) Only LVC	1.02	-0.0266	0.0306	0.00393	0.0877
(iii) Only CLS	2.17	-0.0125	0.0165	0.00395	0.0456
(iv) CLS and LVC	1.11	-0.0080	0.0120	0.00395	0.0320

$S_Z + (7/2)T_Z = 0.20$, which is much smaller than the true value 0.76. This value corresponds to 73% discrepancy, which is larger than 56%, a result of a cluster calculation for $\text{Cr}3d^4$ in an octahedral situation [72]. As mentioned in Sec. III B, the dip and peak around 580–582 eV in the calculated XMCD intensity deviate upward from the experimental ones. This deviation leads to underestimation of the absolute value of negative $\Delta S_{L_3}/S_L$. However, this underestimation seems to be corrected at most by a factor of 2, according to the bottom integrated-intensity curve of Fig. 4, where note that the high-energy cutoff of L_3 excitations is 584 eV. Therefore, if we assume $\Delta S_{L_3}/S_L = -0.016$, then $\Delta S_{L_2}/S_L = 0.020$, and consequently we obtain the estimation $[-\Delta S_{L_3} + 2\Delta S_{L_2}]/S_L = 0.056$. Some experiments have assumed $\text{Cr}3d^2$ ($H_d = 8$), although the calculation gives smaller $H_d = 6.27$. If we use this overestimated $H_d = 8$, we obtain $S_Z + (7/2)T_Z = 0.45$ at most. However, this still reaches only 59% of the true value 0.76. Thus, in the case of CrO_2 , the validity of the spin sum rule cannot be supported within the present analysis. We should note also that $(7/2)T_Z$ is not negligibly small, compared with S_Z . Therefore, extraction of the true spin moment value by means of the spin sum rule is quite problematic, although a correction scheme has been proposed in Ref. [20]. Thus, as well as early local multiplet calculations [70–72], our method based on accurate electron bands can demonstrate the inapplicability of the spin sum rule to early $3d$ transition-metal compounds.

IV. CONCLUDING REMARKS

In this paper we have presented a perturbative method for calculating XAS and XMCD spectra by means of the Keldysh Green's function technique. It is worthwhile to mention the advantages, disadvantages, similarities, and differences of our approach, in comparison with the other approaches reviewed in Ref. [73]. The advantages over LFM or CFM calculations are similar to those of LDA+DMFT method [73]: (i) Charge transfer processes not only from neighboring ligand sites but also from $3d$ states away from the absorbing site are accurately taken into account. (ii) Ambiguities in the choice of model parameters are much reduced since the crystal-field splitting and metal-ligand transfers are almost nonempirically determined by the first-principles band calculations. However, in contrast to the LDA+DMFT approach, our approach (within MFA, GGA, or GGA+ U) does not need mapping to

a corresponding impurity problem and solving it. Therefore, our approach requires only much less cost in numerical calculations than the DMFT approaches. If the MFA Green's functions are replaced with DMFT ones, further effects of electron correlations can be included as well as in DMFT, in exchange for the less cost in calculations. Another remarkable difference from the LDA+DMFT approach is that our approach includes such bound-state-formation processes as described by the Bethe-Salpeter equation (BSE). This will be easily understood, if it is noted that Fig. 2(b) and Eq. (32) are the field-theoretic expression of the BSE, where V_{pd} plays a role of the Bethe-Salpeter kernel. However, it should be noted that our approach differs from the DFT-based BSE approaches reviewed in Refs. [74,75]: In the DFT-based BSE approaches all electrons are involved and the $2p$ - $3d$ interaction is calculated by a first-principles DFT manner, whereas our approach simply includes only the relevant orbitals to the $2p \rightarrow 3d$ XAS process and employs the atomic Hartree-Fock calculation to evaluate the $2p$ - $3d$ interaction. Compared with the LDA+DMFT and DFT-based BSE approaches, our approach requires only less expensive numerical calculations because of the above-mentioned simplicities, thereby making it more feasible to calculate XAS and XMCD intensities in more complex ordering states such as ferrimagnetic states characterized by several kinds of magnetic atoms and ordering wave vectors. A possible disadvantage of our approach is that the Slater-Condon F_{pd} and G_{pd} need to be chosen by a semiempirical way, when the Wannier orbitals are less localized and not similar to atomic orbitals.

Applying our method to half-metallic ferromagnetic CrO_2 , we have obtained XMCD spectral line shapes agreeing well with experiments. We have shown that the atomiclike strong interaction between the $2p$ and $3d$ states is an indispensable ingredient to yield the good agreement. It is suggested that the previous XMCD calculations may have overlooked or underestimated the notable effects of the $2p$ - $3d$ interaction. Concerning the sum rules, it has been demonstrated that while the orbital sum rule holds well, the spin sum rule does not hold, leading to excessive underestimation of the spin moment.

As usually done in local multiplet calculations of XAS [35,61], the Slater-Condon parameters are reduced to 70%–80% of those obtained by atomic Hartree-Fock calculations. Also to our experience, such reduction is often required to yield agreement with experiments. However, in the case of

CrO₂, to obtain the agreement with experiments, we have used the values of F_{pd}^2 , G_{pd}^1 , and G_{pd}^3 without reduction. Necessity of such reduction is considered to arise from a solid-state effect absent in atomic situations, e.g., most possibly a screening caused by conduction electrons. This consideration leads us to the idea that such screening processes are not active sufficiently to weaken the $2p$ - $3d$ Coulomb interaction in CrO₂. This will be plausible if the fact is noted that spin relaxations in HFM are largely suppressed due to the absence of spin-flip processes near the Fermi energy. Therefore, it

may be possible to regard the atomiclike $2p$ - $3d$ interaction as a peculiar feature of HFM. Validity of this perspective on the $2p$ - $3d$ interaction in HFM is still left to be investigated extensively.

ACKNOWLEDGMENT

The authors are much grateful to S. Hamamoto for invaluable communications.

-
- [1] V. Y. Irkhin and M. I. Katsnel'son, Half-metallic ferromagnets, *Phys. Usp.* **37**, 659 (1994).
- [2] J. M. D. Coey and M. Venkatesan, Half-metallic ferromagnetism: Example of CrO₂, *J. Appl. Phys.* **91**, 8345 (2002).
- [3] W. E. Pickett and H. Eschrig, Half metals: from formal theory to real material issues, *J. Phys.: Condens. Matter* **19**, 315203 (2007).
- [4] M. I. Katsnelson, V. Y. Irkhin, L. Chioncel, A. I. Lichtenstein, and R. A. de Groot, Half-metallic ferromagnets: From band structure to many-body effects, *Rev. Mod. Phys.* **80**, 315 (2008).
- [5] K. Schwarz, CrO₂ predicted as a half-metallic ferromagnet, *J. Phys. F: Met. Phys.* **16**, L211 (1986).
- [6] S. Matar, G. Demazeau, J. Sticht, V. Eyert, and J. Kübler, Etude de la structure électronique et magnétique de CrO₂, *J. Phys. I (France)* **2**, 315 (1992).
- [7] S. P. Lewis, P. B. Allen, and T. Sasaki, Band structure and transport properties of CrO₂, *Phys. Rev. B* **55**, 10253 (1997).
- [8] M. A. Korotin, V. I. Anisimov, D. I. Khomskii, and G. A. Sawatzky, CrO₂: A self-doped double exchange ferromagnet, *Phys. Rev. Lett.* **80**, 4305 (1998).
- [9] I. I. Mazin, D. J. Singh, and C. Ambrosch-Draxl, Transport, optical, and electronic properties of the half-metal CrO₂, *Phys. Rev. B* **59**, 411 (1999).
- [10] N. E. Brener, J. M. Tyler, J. Callaway, D. Bagayoko, and G. L. Zhao, Electronic structure and Fermi surface of CrO₂, *Phys. Rev. B* **61**, 16582 (2000).
- [11] H.-T. Jeng and G. Y. Guo, First-principles investigations of the orbital magnetic moments in CrO₂, *J. Appl. Phys.* **92**, 951 (2002).
- [12] L. Craco, M. S. Laad, and E. Müller-Hartmann, Orbital kondo effect in CrO₂: A combined local-spin-density-approximation dynamical-mean-field-theory study, *Phys. Rev. Lett.* **90**, 237203 (2003).
- [13] A. Toropova, G. Kotliar, S. Y. Savrasov, and V. S. Oudovenko, Electronic structure and magnetic anisotropy of CrO₂, *Phys. Rev. B* **71**, 172403 (2005).
- [14] L. Chioncel, H. Allmaier, E. Arrighoni, A. Yamasaki, M. Daghofer, M. I. Katsnelson, and A. I. Lichtenstein, Half-metallic ferromagnetism and spin polarization in CrO₂, *Phys. Rev. B* **75**, 140406(R) (2007).
- [15] I. V. Solovyev, I. V. Kashin, and V. V. Mazurenko, Mechanisms and origins of half-metallic ferromagnetism in CrO₂, *Phys. Rev. B* **92**, 144407 (2015).
- [16] Y. Ji, G. J. Strijkers, F. Y. Yang, C. L. Chien, J. M. Byers, A. Anguelouch, G. Xiao, and A. Gupta, Determination of the spin polarization of half-metallic CrO₂ by point contact Andreev reflection, *Phys. Rev. Lett.* **86**, 5585 (2001).
- [17] J. S. Parker, S. M. Watts, P. G. Ivanov, and P. Xiong, Spin polarization of CrO₂ at and across an artificial barrier, *Phys. Rev. Lett.* **88**, 196601 (2002).
- [18] H. Fujiwara, M. Sunagawa, K. Terashima, T. Kittaka, T. Wakita, Y. Muraoka, and T. Yokoya, Intrinsic spin polarized electronic structure of CrO₂ epitaxial film revealed by bulk-sensitive spin-resolved photoemission spectroscopy, *Appl. Phys. Lett.* **106**, 202404 (2015).
- [19] J. Stöhr, X-ray magnetic circular dichroism spectroscopy of transition metal thin films, *J. Electron. Spectrosc. Relat. Phenom.* **75**, 253 (1995).
- [20] E. Goering, X-ray magnetic circular dichroism sum rule correction for the light transition metals, *Philos. Mag.* **85**, 2895 (2005).
- [21] T. Nakamura and M. Suzuki, Recent progress of the x-ray magnetic circular dichroism technique for element-specific magnetic analysis, *J. Phys. Soc. Jpn.* **82**, 021006 (2013).
- [22] G. van der Laan and A. I. Figueroa, X-ray magnetic circular dichroism—A versatile tool to study magnetism, *Coord. Chem. Rev.* **277–278**, 95 (2014).
- [23] B. T. Thole, P. Carra, F. Sette, and G. van der Laan, X-ray circular dichroism as a probe of orbital magnetization, *Phys. Rev. Lett.* **68**, 1943 (1992).
- [24] P. Carra, B. T. Thole, M. Altarelli, and X. Wang, X-ray circular dichroism and local magnetic fields, *Phys. Rev. Lett.* **70**, 694 (1993).
- [25] K. Attenkofer and G. Schütz, Hard and soft X-MCD studies of CrO₂, *J. Phys. IV (France)* **7**, C2-459 (1997).
- [26] D. J. Huang, H. T. Jeng, C. F. Chang, G. Y. Guo, J. Chen, W. P. Wu, S. C. Chung, S. G. Shyu, C. C. Wu, H.-J. Lin, and C. T. Chen, Orbital magnetic moments of oxygen and chromium in CrO₂, *Phys. Rev. B* **66**, 174440 (2002).
- [27] E. Goering, A. Bayer, S. Gold, G. Schütz, M. Rabe, U. Rüdiger, and G. Güntherodt, Direct correlation of Cr $3d$ orbital polarization and O K -edge x-ray magnetic circular dichroism of epitaxial CrO₂ films, *Europhys. Lett.* **58**, 906 (2002); Strong anisotropy of projected $3d$ moments in epitaxial CrO₂ films, *Phys. Rev. Lett.* **88**, 207203 (2002).
- [28] S. Gold, E. Goering, C. König, U. Rüdiger, G. Güntherodt, and G. Schütz, Temperature dependence of the magnetocrystalline anisotropy energy and projected microscopic magnetic moments in epitaxial CrO₂ films, *Phys. Rev. B* **71**, 220404(R) (2005).

- [29] M. Pathak, H. Sims, K. B. Chetry, D. Mazumdar, P. R. LeClair, G. J. Mankey, W. H. Butler, and A. Gupta, Robust room-temperature magnetism of (110) CrO₂ thin films, *Phys. Rev. B* **80**, 212405 (2009).
- [30] S. Seong, E. Lee, H. W. Kim, B. I. Min, S. Lee, J. Dho, Y. Kim, J. Y. Kim, and J. S. Kang, Experimental evidence for mixed-valent Cr ions in half-metallic CrO₂: Temperature-dependent XMCD study, *J. Magn. Magn. Mater.* **452**, 447 (2018).
- [31] F. de Groot and A. Kotani, *Core Level Spectroscopy of Solids* (CRC Press, Boca Raton, FL, 2008), p. 297.
- [32] V. Kanchana, G. Vaitheeswaran, and M. Alouani, Calculated electronic structure and x-ray magnetic circular dichroism of CrO₂, *J. Phys.: Condens. Matter* **18**, 5155 (2006).
- [33] N. Baadji, M. Alouani, and H. Dreyssé, Calculated magnetic x-ray circular dichroism of half-metal CrO₂, *Europhys. Lett.* **87**, 27004 (2009).
- [34] B. Loukya, X. Zhang, A. Gupta, and R. Datta, Electron magnetic chiral dichroism in CrO₂ thin films using monochromatic probe illumination in a transmission electron microscope, *J. Magn. Magn. Mater.* **324**, 3754 (2012).
- [35] J. Zaanen, G. A. Sawatzky, J. Fink, W. Speier, and J. C. Fuggle, $L_{2,3}$ absorption spectra of the lighter 3d transition metals, *Phys. Rev. B* **32**, 4905 (1985).
- [36] J. Schwitalla and H. Ebert, Electron core-hole interaction in the x-ray absorption spectroscopy of 3d transition metals, *Phys. Rev. Lett.* **80**, 4586 (1998).
- [37] A. L. Ankudinov, A. I. Nesvizhskii, and J. J. Rehr, Dynamic screening effects in x-ray absorption spectra, *Phys. Rev. B* **67**, 115120 (2003).
- [38] R. Laskowski and P. Blaha, Understanding the $L_{2,3}$ x-ray absorption spectra of early 3d transition elements, *Phys. Rev. B* **82**, 205104 (2010).
- [39] P. Blaha, K. Schwarz, G. K. H. Madsen, D. Kvasnicka, J. Luitz, R. Laskowski, F. Tran, and L. D. Marks, *WIEN2K, An Augmented Plane Wave Plus Local Orbitals Program for Calculating Crystal Properties* (Techn. Universität Wien, Austria, 2023).
- [40] N. Marzari, A. A. Mostofi, J. R. Yates, I. Souza, and D. Vanderbilt, Maximally localized Wannier functions: Theory and applications, *Rev. Mod. Phys.* **84**, 1419 (2012).
- [41] G. Pizzi, V. Vitale, R. Arita, S. Blügel, F. Freimuth, G. Géranton, M. Gibertini, D. Gresch, C. Johnson, T. Koretsune, J. Ibañez-Azpiroz, H. Lee, J.-M. Lihm, D. Marchand, A. Marrazzo, Y. Mokrousov, J. I. Mustafa, Y. Nohara, Y. Nomura, L. Paulatto *et al.*, Wannier90 as a community code: new features and applications, *J. Phys.: Condens. Matter* **32**, 165902 (2020).
- [42] B. J. Thamer, R. M. Douglass, and E. Staritzky, The thermal decomposition of aqueous chromic acid and some properties of the resulting solid phases, *J. Am. Chem. Soc.* **79**, 547 (1957).
- [43] W. H. Cloud, D. S. Schreiber, and K. R. Babcock, X-ray and magnetic studies of CrO₂ single crystals, *J. Appl. Phys.* **33**, 1193 (1962).
- [44] P. Porta, M. Marezio, J. P. Remeika, and P. D. Dernier, Chromium dioxide: High pressure synthesis and bond lengths, *Mater. Res. Bull.* **7**, 157 (1972).
- [45] J. P. Perdew, K. Burke, and M. Ernzerhof, Generalized gradient approximation made simple, *Phys. Rev. Lett.* **77**, 3865 (1996).
- [46] T. Tsujioka, T. Mizokawa, J. Okamoto, A. Fujimori, M. Nohara, H. Takagi, K. Yamaura, and M. Takano, Hubbard splitting and electron correlation in the ferromagnetic metal CrO₂, *Phys. Rev. B* **56**, R15509 (1997).
- [47] C. F. Chang, D. J. Huang, A. Tanaka, G. Y. Guo, S. C. Chung, S.-T. Kao, S. G. Shyu, and C. T. Chen, Electronic structure of CrO₂ studied by magnetic circular dichroism in resonant photoemission, *Phys. Rev. B* **71**, 052407 (2005).
- [48] M. Sperlich, C. König, G. Güntherodt, A. Sekiyama, G. Funabashi, M. Tsunekawa, S. Imada, A. Shigemoto, K. Okada, A. Higashiya, M. Yabashi, K. Tamasaku, T. Ishikawa, V. Renken, T. Allmers, M. Donath, and S. Suga, Intrinsic correlated electronic structure of CrO₂ revealed by hard x-ray photoemission spectroscopy, *Phys. Rev. B* **87**, 235138 (2013).
- [49] F. Bisti, V. A. Rogalev, M. Karolak, S. Paul, A. Gupta, T. Schmitt, G. Güntherodt, V. Eyert, G. Sangiovanni, G. Profeta, and V. N. Strocov, Weakly-correlated nature of ferromagnetism in nonsymmorphic CrO₂ revealed by bulk-sensitive soft-x-ray ARPES, *Phys. Rev. X* **7**, 041067 (2017).
- [50] See Supplemental Material at <http://link.aps.org/supplemental/10.1103/PhysRevB.109.184414> for (1) Electronic structures by MFA, GGA, and GGA+ U (see also Refs. [18,39–41,49,51–55]), (2) XAS of Cr₂O₃ (see also Refs. [56–59]), (3) XMCD spectra by GGA and GGA+ U , and (4) data availability.
- [51] G. K. H. Madsen and P. Novak, Charge order in magnetite. An LDA+ U study, *Europhys. Lett.* **69**, 777 (2005); http://susi.theochem.tuwien.ac.at/reg_user/textbooks/Constraint_U.pdf.
- [52] R. Tesch and P. M. Kowalski, Hubbard U parameters for transition metals from first principles, *Phys. Rev. B* **105**, 195153 (2022), and references therein.
- [53] G. C. Moore, M. K. Horton, E. Linscott, A. M. Ganose, M. Siron, D. D. O'Regan, and K. A. Persson, High-throughput determination of Hubbard U and Hund J values for transition metal oxides via the linear response formalism, *Phys. Rev. Mater.* **8**, 014409 (2024), and references therein.
- [54] G. Kresse and J. Furthmüller, Efficient iterative schemes for *ab initio* total-energy calculations using a plane-wave basis set, *Phys. Rev. B* **54**, 11169 (1996); J. Hafner, *Ab-initio* simulations of materials using VASP: Density-functional theory and beyond, *J. Comput. Chem.* **29**, 2044 (2008).
- [55] I. Carnimeo, F. Affinito, S. Baroni, O. Baseggio, L. Bellentani, R. Bertossa, P. D. Delugas, F. F. Ruffino, S. Orlandini, F. Spiga, and P. Giannozzi, Quantum ESPRESSO: One further step toward the exascale, *J. Chem. Theory Comput.* **19**, 6992 (2023).
- [56] L. W. Finger and R. M. Hazen, Crystal structure and isothermal compression of Fe₂O₃, Cr₂O₃, and V₂O₃ to 50 kbars, *J. Appl. Phys.* **51**, 5362 (1980).
- [57] L. M. Corliss, J. M. Hastings, R. Nathans, and G. Shirane, Magnetic structure of Cr₂O₃, *J. Appl. Phys.* **36**, 1099 (1965).
- [58] Yu. S. Dedkov, A. S. Vinogradov, M. Fonin, C. König, D. V. Vyalikh, A. B. Preobrajenski, S. A. Krasnikov, E. Yu. Kleimenov, M. A. Nesterov, U. Rüdiger, S. L. Molodtsov, and G. Güntherodt, Correlations in the electronic structure of half-metallic ferromagnetic CrO₂ films: An x-ray absorption and resonant photoemission spectroscopy study, *Phys. Rev. B* **72**, 060401(R) (2005).
- [59] C. Theil, J. van Elp, and F. Folkmann, Ligand field parameters obtained from and chemical shifts observed at the Cr $L_{2,3}$ edges, *Phys. Rev. B* **59**, 7931 (1999).

- [60] R. D. Cowan, *The Theory of Atomic Structure and Spectra* (University of California Press, Berkeley, 1981).
- [61] F. M. F. de Groot, J. C. Fuggle, B. T. Thole, and G. A. Sawatzky, $2p$ x-ray absorption of $3d$ transition-metal compounds: An atomic multiplet description including the crystal field, *Phys. Rev. B* **42**, 5459 (1990).
- [62] J. J. Sakurai, *Advanced Quantum Mechanics* (Addison Wesley, Boston, 1967), Secs. 2-4 and 4-1 for the electric-dipole approximation and natural units, respectively.
- [63] L. V. Keldysh, Diagram technique for nonequilibrium processes, *J. Exptl. Theoret. Phys. (U.S.S.R.)* **47**, 1515 (1964) [*Sov. Phys. JETP* **20**, 1018 (1965)].
- [64] A. Koide, T. Nomura, and T. Inami, Effects of conduction electron excitation on x-ray magnetic circularly polarized emission in itinerant ferromagnets, *Phys. Rev. B* **102**, 224425 (2020).
- [65] H. Kobayashi, A. Koide, T. Nomura, and T. Inami, Comparative theoretical study of x-ray magnetic circularly polarized emission from ferromagnetic Fe, Co, and Ni, *Europhys. Lett.* **140**, 36002 (2022).
- [66] M. Komelj, C. Ederer, and M. Fähnle, Anisotropy of orbital moments and magnetic dipole term T_z in CrO_2 : An *ab initio* study, *Phys. Rev. B* **69**, 132409 (2004).
- [67] W. L. O'Brien and B. P. Tonner, Orbital and spin sum rules in x-ray magnetic circular dichroism, *Phys. Rev. B* **50**, 12672 (1994).
- [68] R. Wu and A. J. Freeman, Limitation of the magnetic-circular-dichroism spin sum rule for transition metals and importance of the magnetic dipole term, *Phys. Rev. Lett.* **73**, 1994 (1994).
- [69] C. T. Chen, Y. U. Idzerda, H.-J. Lin, N. V. Smith, G. Meigs, E. Chaban, G. H. Ho, E. Pellegrin, and F. Sette, Experimental confirmation of the x-ray magnetic circular dichroism sum rules for iron and cobalt, *Phys. Rev. Lett.* **75**, 152 (1995).
- [70] Y. Teramura, A. Tanaka, and T. Jo, Effect of coulomb interaction on the x-ray magnetic circular dichroism spin sum rule in $3d$ transition elements, *J. Phys. Soc. Jpn.* **65**, 1053 (1996).
- [71] C. Piamonteze, P. Miedema, and F. M. F. de Groot, Accuracy of the spin sum rule in XMCD for the transition-metal L edges from manganese to copper, *Phys. Rev. B* **80**, 184410 (2009).
- [72] J. P. Crocombette, B. T. Thole, and F. Jollet, The importance of the magnetic dipole term in magneto-circular x-ray absorption dichroism for $3d$ transition metal compounds, *J. Phys.: Condens. Matter* **8**, 4095 (1996).
- [73] F. M. F. de Groot, H. Elnaggar, F. Frati, R. Wang, M. U. Delgado-Jaime, M. van Veenendaal, J. Fernandez-Rodriguez, M. W. Haverkort, R. J. Green, G. van der Laan, Y. Kvashnin, A. Hariki, H. Ikeno, H. Ramanantoanina, C. Daul, B. Delley, M. Odelius, M. Lundberg, O. Kuhn, S. I. Bokarev *et al.*, $2p$ x-ray absorption spectroscopy of $3d$ transition metal systems, *J. Electron. Spectrosc. Relat. Phenom.* **249**, 147061 (2021).
- [74] K. Gilmore, J. Vinson, E. L. Shirley, D. Prendergast, C. D. Pemmaraju, J. J. Kas, F. D. Vila, and J. J. Rehr, Efficient implementation of core-excitation Bethe-Salpeter equation calculations, *Comput. Phys. Commun.* **197**, 109 (2015).
- [75] C. Vorwerk, B. Aurich, C. Cocchi and C. Draxl, Bethe-Salpeter equation for absorption and scattering spectroscopy: implementation in the exciting code, *Electron. Struct.* **1**, 037001 (2019).